RSC Advances

PAPER

View Article Online
View Journal | View Issue

Cite this: *RSC Adv.*, 2026, **16**, 16653

Sb_2Se_3/CdSe thin film photocathode for efficient hydrogen production

Liting Wei,* Yinhu Yu, Tong Chang, Jiao Jiao and Yangfang Wu

A highly efficient narrow-band-gap photoelectrode plays a vital role in achieving solar-to-hydrogen conversion. In this work, we report a novel Sb_2Se_3/CdSe/Pt photocathode, and the activity of this photocathode was studied. The photocathode was fabricated *via* electrodeposition followed by annealing and surface modification with a CdSe monolayer and Pt cocatalyst. The photocurrent density of the Sb_2Se_3/CdSe/Pt photocathode is *ca.* −6.9 mA cm^{-2} at −0.2 V_{RHE} in near-neutral pH buffered solution, which is 2.3 times that of the Sb_2Se_3/Pt photoelectrode. The enhanced photoelectrochemical (PEC) performance is owing to the successful construction of the Sb_2Se_3/CdSe p–n heterojunction, which contributes to effective charge separation and transfer. Additionally, the effect of the Sb_2Se_3 layer thickness on the photocurrent was investigated, which suggests that an appropriate thickness of Sb_2Se_3 layer is necessary for sufficient light absorption and efficient hole transport. This work develops a novel Sb_2Se_3-based p–n heterojunction photocathode using a facile fabrication approach, which provides a practical pathway for developing cost-effective PEC devices with wide solar spectrum utilization.

Received 6th January 2026
Accepted 16th March 2026

DOI: 10.1039/d6ra00129g

rsc.li/rsc-advances

1. Introduction

Photoelectrochemical hydrogen production *via* water splitting is one of the most promising and challenging techniques for sustainable solar energy storage,[1,2] and utilizes semiconductor materials as photoelectrodes, enabling the direct conversion of solar energy into storable hydrogen. Sb_2Se_3, as a low-band-gap (1.2–1.0 eV) semiconductor, has been attracting tremendous interest due to its exceptional optoelectronic properties and material advantages. The narrow band gap and high absorption coefficient ($\sim 10^5$ cm^{-1} near the absorption edge) of Sb_2Se_3 enable broad and efficient solar harvesting.[3–5] Furthermore, Sb_2Se_3 has economic and environmental benefits, including earth abundance, low cost comparable to copper, and non-toxicity. Crucially, the Sb–Se phase diagram contains only one binary compound, namely orthogonal Sb_2Se_3,[6] which makes it easier to control the phase and defects compared with multinary chalcogenides like Cu(In,Ga)$(S,Se)_2$ and $Cu_2ZnSn(S,Se)_4$.[7,8] In addition, the high electron mobility (16.9 cm^2 V^{-1} S^{-1}) of Sb_2Se_3 (ref. 9) is conducive to charge transport in thick films, simultaneously minimizing recombination losses and maximizing light absorption.

The performance of the Sb_2Se_3 photocathode is significantly influenced by the fabrication method, and there are multiple approaches available for preparing Sb_2Se_3 photocathodes. The photocurrent density of the Sb_2Se_3 film prepared *via* solution-based approaches can reach −13 mA cm^{-2} at 0 V_{RHE}, but this method depends on dissolving the Sb source and the Se source in toxic organic solvents, such as hydrazine hydrate, TGA and 2-mercaptoethanol, and the uniformity in the photocathode films is also an issue for scaling up the method.[10–12] Besides, the low melting point of Sb_2Se_3 (*ca.* 600 °C) and its high saturated vapor pressure (*ca.* 1200 Pa at 550 °C)[6] enable Sb_2Se_3 thin-film deposition *via* thermal evaporation technology.[13,14] However, the quality of film by thermal deposition technology is easily affected by the distance between the evaporation source and the substrate, the temperature of the substrate, and the interface properties, which are difficult to control.[15,16] Among the various film fabrication techniques, the electrodeposition method is the most promising in terms of scalability and operability.[17] By varying solution composition and electrodeposition parameters, the morphology and thickness can be tuned under ambient conditions, making this approach economical and practical. Despite these advantages, minimal efforts have been made to synthesize Sb_2Se_3 photocathode by the electrodeposition method and use them for photoelectrochemical applications.

To improve the PEC water splitting performance, typical n-type semiconductors (*e.g.*, CdS,[14] In_2S_3,[18] TiO_2 (ref. 19)) are deposited onto p-type substrates as a buffer layer, thus establishing p–n junctions to enhance charge separation and suppress charge recombination. Among the n-type semiconductors, CdSe stands out due to its favorable band structure alignment and superior charge transport properties,[20] making it a promising candidate for PEC applications.[21,22] Consequently, engineering an Sb_2Se_3/CdSe heterojunction photocathode

Department of Applied Chemistry, Yuncheng University, Yuncheng 044000, China. E-mail: weiliting_job@163.com

represents an effective strategy for achieving high-performance PEC water splitting.

Based on the above considerations, Sb_2Se_3-based thin-film photocathode for PEC water splitting was fabricated *via* a three-step process: electrodeposition in an alkaline selenosulfate electrolyte, followed by appropriate annealing, and rational surface engineering with a CdSe layer and Pt catalyst. A photocurrent density of 6.9 mA cm^{-2} has been achieved for Sb_2Se_3/CdSe/Pt photocathode at −0.2 V_{RHE} in a near-neutral electrolyte. The influence of the Sb_2Se_3 layer thickness on the PEC performance is analyzed, which suggests that an appropriate thickness of Sb_2Se_3 layer is necessary for sufficient light absorption and efficient holes transport. The novel Sb_2Se_3-based p–n heterojunction photocathode with efficient PEC performance and scalable fabrication method demonstrates the great potential of developing cost-effective PEC devices with wide solar-spectrum utilization for H_2 evolution.

2 Experimental

2.1 Fabrication of Sb_2Se_3 film

The electrolyte consists of an ammonia buffer aqueous solution (0.1 M, pH = 9.0) containing sodium selenosulfate and antimony complex. Sodium selenosulfate solution was prepared *via* a modified literature method.[20] Briefly, Se powder(0.789 g), Na_2SO_3(3.15 g) and deionized water (50 mL) were added to a three-necked round bottom flask, purged with N_2 for 20 minutes, then refluxed at 70 °C for 10 hours to obtain Na_2SeSO_3 solution. Meanwhile, $C_8H_4K_2O_{12}Sb_2 \cdot 3H_2O$ (1.25 mM) was dissolved separately in the ammonium buffer solution. The final electrolyte was obtained by mixing both solutions at a volume ratio of 7 : 3, followed by Ar purging for 15 minutes. Electrochemical deposition was conducted using a CHI 760 D electrochemical workstation in a three-electrode configuration, with commercial FTO-coated glass, Pt foil, and saturated calomel electrode (SCE) as the working electrode, the counter electrode, and the reference electrode, respectively. Potentiostatic electrodeposition at −0.94 V_{SCE} is carried out,[21] with charge density passed ranging from 0.125–1.0C cm^{-2}. Post-deposition annealing treatments were conducted at 200 °C–300 °C for 20 min using a rapid heating furnace.

2.2 Chemical bath deposition (CBD) of CdSe

In a separate beaker, KOH(0.505 g) was added into 100 mL deionized water, then nitrilotriacetic acid (0.57 g) was added into the above solution until all KOH is dissolved. Subsequently, $Cd(NO_3)_2 \cdot 4H_2O$(0.617 g) was added into the above solution with magnetic stirring for 20 min. The Sb_2Se_3/FTO was placed into the above transparent solution and leaned against the wall of the beaker, followed by blowing N_2 for 20 minutes and keeping it in a 70 °C water bath for 10 minutes. Finally, 10 mL of Na_2SeSO_3 solution was quickly transferred to the above solution and then kept for 1 hour. The obtained samples were washed with DI water and dried in vacuum.

2.3 Photo-assisted electrodeposition of Pt

Pt nanoparticles were deposited by photo-assisted electrodeposition method in a solution containing 0.1 mM $H_2PtCl_6 \cdot 6H_2O$ (99.9% metals basis) and 0.5 M Na_2SO_4. Each deposition was performed at a fixed potential of 0 V_{RHE} under simulated sunlight (AM 1.5 G) from a 300 W Xe lamp solar simulator with magnetic stirring.

2.4 Photoelectrochemical measurements

The PEC measurements were performed with a conventional three-electrode configuration in phosphate buffered solution (pH = 6.5, containing 0.5 M Na_2SO_4, 0.25 M Na_2HPO_4/NaH_2PO_4) under AM 1.5 G sunlight illumination. The light intensity at the electrode is controlled to 100 mW cm^{-2}. The measured potential ($V_{Ag/AgCl}$) could convert to reversible hydrogen electrode potential (V_{RHE}) using the Nernst equation: $V_{RHE} = V_{Ag/AgCl} + 0.059\ pH + 0.197$. The Mott–Schottky plots were acquired at a frequency of 2 KHz in the darkness. The electrochemical impedance spectroscopy (EIS) tests were performed at 0 V_{RHE} within a frequency of 1 Hz to 100 KHz.

2.5 Materials characterizations

X-ray diffraction (XRD) was conducted to analyze the crystallographic structure of the samples using an X-ray diffractometer with Cu Kα radiation. Scanning electron microscope (JEOL JSM 7800 FE) equipped with energy dispersive X-ray spectroscope (EDX) was employed to observe the morphology and elemental distribution of the photoelectrode. Optical absorption properties of the films were measured with a spectrophotometer (Cary 5000, Agilent). The optical absorption (A) of the films was calculated using the formula: $A = 100 - T - R$, where T denotes transmittance and R corresponds to reflectance.

3. Results and discussion

3.1 Fabrication and surface modification of Sb_2Se_3 thin films

As shown in Fig. 1a, the Sb_2Se_3 film was grown onto a FTO coated glass substrate by facile electrodeposition, which was then annealed to obtain a high-quality polycrystalline thin film. Then, the surface of the annealed-Sb_2Se_3 thin film was modified with n-type CdSe *via* CBD to form a p–n junction. The deposited Sb_2Se_3 (Fig. 1c), 250 °C annealed Sb_2Se_3 (Fig. 1d) and CdSe-modified 250 °C annealed Sb_2Se_3 (Fig. 1e) exhibits macroscopic homogeneity. XRD patterns were obtained to analyze the phase composition and structure. As shown in Fig. S1, the deposited Sb_2Se_3 film exhibits no obvious diffraction peaks apart from those originating from the FTO substrate, implying the amorphous structure for the deposited Sb_2Se_3 films. In contrast, all annealed Sb_2Se_3 films display sharp diffraction peaks matching the orthorhombic Sb_2Se_3 (PDF No. 15-0861),[22] demonstrating that thermal annealing is essential for inducing the structural transformation from disordered amorphous state to well-ordered crystalline phase. Annealed Sb_2Se_3 film is comprised of densely packed spherical particles with an average size of *ca.* 100 nm (Fig. 1h). After modification with CdSe,

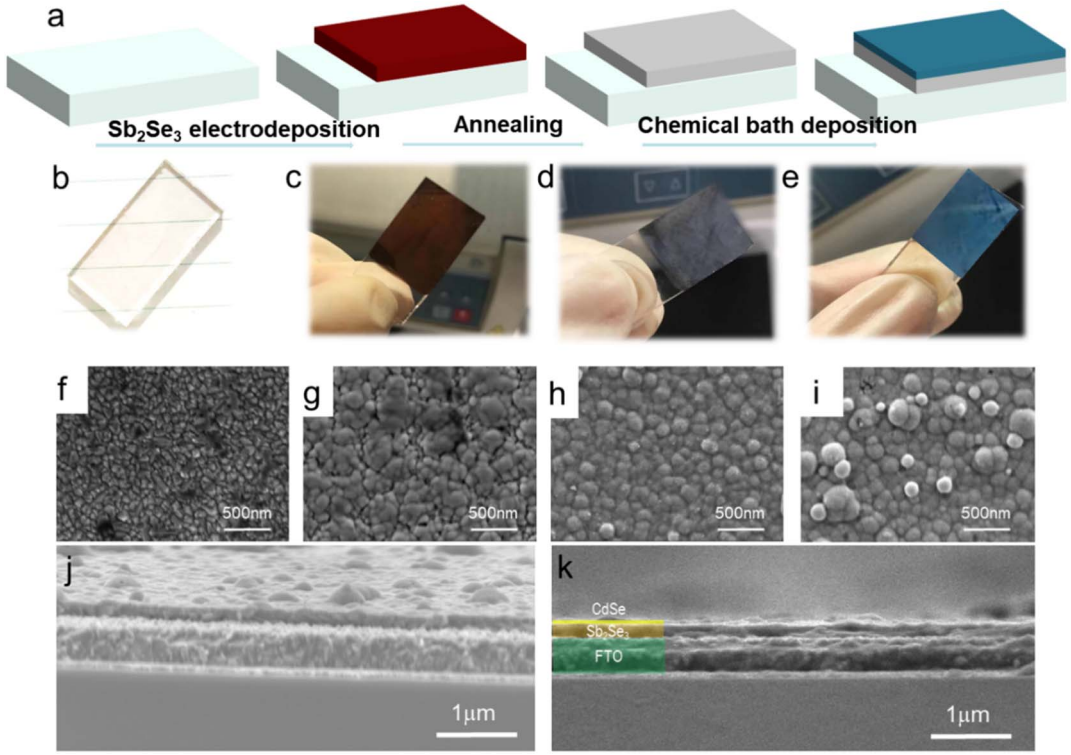

Fig. 1 (a) Schematic diagram of fabrication process for Sb_2Se_3/CdSe. (b–e) Optical images of the FTO substrate, deposited Sb_2Se_3, 250 °C annealed Sb_2Se_3, and Sb_2Se_3/CdSe. (f–i) Top-view SEM images of the FTO substrate, deposited Sb_2Se_3, 250 °C annealed Sb_2Se_3, and Sb_2Se_3/CdSe. (j and k) Cross-sectional SEM images of the Sb_2Se_3 and Sb_2Se_3/CdSe.

a uniform CdSe overlayer is formed on the surface (Fig. 1i). XRD patterns for Sb_2Se_3/CdSe are presented in Fig. S2. It is observed that the new peaks occurred at 25.3°, 42.2°, and 49.7°, corresponding to the (111), (220), and (311) planes of cubic CdSe.[23] Fig. S3 shows that CdSe particles with an average particle size of 70 nm are uniformly distributed on FTO. The EDS elemental mappings further verify the homogeneous distribution of Sb, Se and Cd elements across the film (Fig. S4). The cross-sectional SEM image reveals that the deposited Sb_2Se_3 layer with a thickness of *ca.* 140 nm covers the FTO substrate (Fig. 1j). For the CdSe-modified Sb_2Se_3 film (Fig. 1k), a CdSe overlayer with a thickness of *ca.* 20 nm coats the underlying Sb_2Se_3 film.

3.2 Effect of calcination temperature on PEC properties of Sb_2Se_3-Based electrodes

The PEC performance of Sb_2Se_3-based electrodes was investigated under simulated sunlight (AM 1.5 G). As shown in Fig. 2a, the bare p-type Sb_2Se_3 electrodes annealed at 200–300 °C displays low cathodic photocurrents of only tens of μA cm^{-2}. The poor PEC activity of unmodified p-type Sb_2Se_3 photoelectrodes implies the necessity of further enhancement through rational interface engineering. After the surface decoration of Pt nanoparticles (Fig. 2b), the photocurrent densities are significantly enhanced. Particularly, the Sb_2Se_3/Pt photocathode annealed at 250 °C achieves the highest photocurrent density (J_{ph}) of *ca.* −3.0 mA cm^{-2} at −0.2 V_{RHE}. The charge transfer rate during the photoelectrochemical reaction was explored by EIS measurements. As shown in Fig. 2c, the Nyquist curves of Sb_2Se_3/Pt show an approximate semicircle, which are fitted using an *R* (CR) circuit (see inset of the Fig. 2c). R_s, R_{ct}, CPE_1 correspond to solution resistance, charge transfer resistance and capacitance. It is observed that 250 °C annealed Sb_2Se_3/Pt has the lower R_{ct} (1904 Ω cm^2) under illumination conditions than the R_{ct} of 200 °C and 300 °C annealed sample (2714 and 2506 Ω cm^2), indicating the effective charge transfer and separation at the electrode–electrolyte interface on the Sb_2Se_3/Pt electrode annealed at 250 °C.

Mott–Schottky measurements were carried out to determine the carrier density (N_d). N_d can be calculated from the M–S slope using the following equation:

$$N_d = \frac{2}{e_0 \varepsilon_0 \varepsilon}\left[\frac{d(1/C^2)}{dV}\right]^{-1}$$

where e_0, ε_0 and ε are the charge of an electron, vacuum permittivity and the relative dielectric constant, respectively. $\frac{d(1/C^2)}{dV}$ is the slope of the Mott–Schottky plot.[24,25] Assuming equivalent ε for all the samples, a larger Mott–Schottky slope corresponds to a lower carrier density. Relevant parameters are summarized in Table S1. As shown in Fig. 2d, the slope of the M–S plots for the sample annealed at 250 °C reaches the minimum, leading to the higher density of trapped electrons, which can be explained by the XRD and SEM results. The lower annealed temperature (200 °C) induces a lower crystallinity

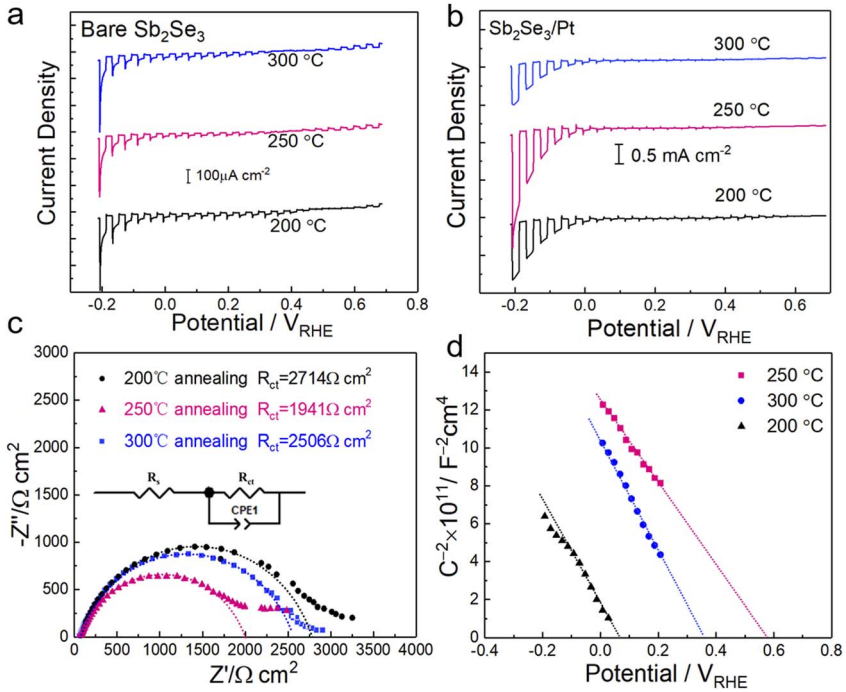

Fig. 2 LSV plots of (a) bare Sb_2Se_3 and (b) Sb_2Se_3/Pt photocathodes. The Sb_2Se_3 samples were calcined at 200, 250 and 300 °C. (c) Nyquist plots of Sb_2Se_3/Pt electrodes conducted at 0 V_{RHE} under illuminated conditions and (d) Mott–Schottery plots of Sb_2Se_3 under darkness condition.

(Fig. S5), thus reducing the electron mobility. Conversely, the excessively high annealing temperature can result in the volatilization of Se, thus generating numerous Se vacancies. These vacancies serve as recombination centers that can trap the photogenerated carriers, ultimately deteriorating the performance of PEC device, which is consistent with observations in previously reported Ar-annealed Sb_2Se_3 thin-film solar cells.[13] As shown in Fig. S5c and f, Sb_2Se_3 film annealed at 300 °C exhibits obvious pores on the surface, indicating that vaporization occurs at the temperature, which results in the decomposition of performance. Based on the transmittance spectrum of 250 °C annealed Sb_2Se_3 (Fig. S6), the direct band gap is determined to be 1.33 eV.

Table 1 compares the performance of Sb_2Se_3 thin films prepared by different fabrication methods including electrodeposition, thermal evaporation and spin coating. Sb_2Se_3 film prepared by electrodeposition achieved a photocurrent of 30 μA cm^{-2}, which is comparable with that obtained by other methods. Therefore, Sb_2Se_3 thin films produced by electrodeposition along with a moderate annealing offers a competitive balance of PEC performance, operability, and cost-effectiveness. However, further enhancement on the photocurrent is required to catch up the state-of-the-art photocathodes. To address this limitation, CdSe layer is introduced to form a beneficial p–n heterojunction with Sb_2Se_3, as discussed in the following section.

3.3 Effect of CdSe on PEC properties of Sb_2Se_3-Based electrodes

To explore the effect of modified CdSe layer on the PEC performance, the LSV measurements were examined. As shown in Fig. 3a, the Sb_2Se_3/CdSe/Pt photocathode generates superior PEC performance, achieving a high J_{ph} of −6.9 mA cm^{-2} at −0.2 V_{RHE} and a large onset potential (V_{on}) of 0.004 V_{RHE} (defined as the voltage at which the J_{ph} reaching −0.5 mA cm^{-2}). In a sharp comparison, the bare Sb_2Se_3 electrode showed a very weak cathodic current (tens of μA cm^{-2}) (Fig. 1a) due to severe charge recombination and sluggish HER kinetics. Although depositing Pt as a cocatalyst, the J_{ph} only reached −3.0 mA cm^{-2} at −0.2 V_{RHE} for Sb_2Se_3/Pt photocathode, with a less positive V_{on} of −0.1 V_{RHE}. Fig. S7 displays statistical distribution of J_{ph} and V_{on} for Sb_2Se_3/Pt and Sb_2Se_3/CdSe/Pt photoelectrodes, proving satisfactory reproducibility. To further elucidate the underlying mechanism of charge transfer and separation, transient photocurrent measurements were carried out. As shown in Fig. 3b, both two *J–T* curves show an observable 'spike-like'

Table 1 The comparison of PEC performance of this work with other Sb_2Se_3 electrodes

Photoelectrodes	Preparation method	Test condition	Photocurrent at 0 V_{RHE}/μA cm^{-2}	Reference
Sb_2Se_3	Electrodeposition	Nea-neutral electrolyte	30	This work
Sb_2Se_3	Thermal evaporation	Nea-neutral electrolyte	~2	22
Sb_2Se_3	Spin coating	0.5 M H_2SO_4 electrolyte	~90	26

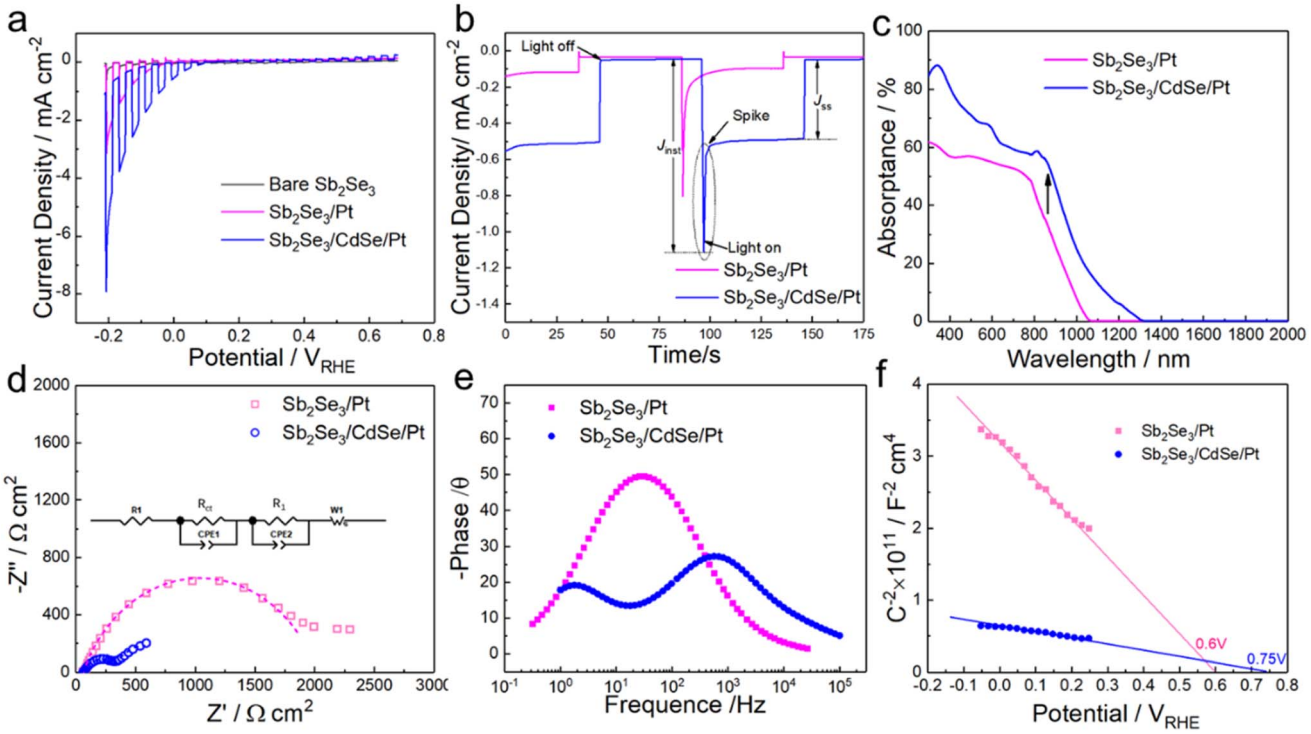

Fig. 3 (a) LSV curves of bare Sb_2Se_3, Sb_2Se_3/Pt and Sb_2Se_3/CdSe/Pt photoelectrodes. (b) Transient photocurrent response and (c) absorption spectra for the as-obtained samples. (d) Nyquist plots, and (e) the corresponding Bode plots of Sb_2Se_3/Pt and Sb_2Se_3/CdSe/Pt obtained at 0 V_{RHE} under illumination. (f) Mott–Schottery plots of different photocathodes without illumination.

transient, *i.e.*, a rapid initial increase in photocurrent upon illumination, followed by a decay to a steady-state value, meaning much electrons being trapped. According to the proportion of the steady-state photocurrent (J_{ss}) and the instantaneous photocurrent (J_{ss}), the charge transfer efficiency (η_{tran}) values of Sb_2Se_3/Pt and Sb_2Se_3/CdSe/Pt devices were determined to be 12.3% and 44.1%, respectively. Based on the light-harvesting efficiency (Fig. S8) derived from wavelength-dependent absorbance (Fig. 3c) and AM 1.5 G solar spectrum (Fig. S9), the calculated η_{sep} value for Sb_2Se_3/CdSe/Pt device (6.2%) is higher than Sb_2Se_3/Pt (4.1%).[27,28] Fig. S9 illustrates that the theoretical photocurrent density (J_{abs}) values for the two photocathodes are very close, being 18.8 mA cm^{-2}. Notably, the experimentally obtained J_{ph} of 0.5 mA cm^{-2} is much lower than its corresponding J_{abs} value of 18.8 mA cm^{-2}, which is owing to the limited carrier dynamics.

To elucidate the interface charge transfer process, EIS measurements were performed on the Sb_2Se_3/CdSe photoelectrode. As shown in Fig. 3d, the Nyquist plot of Sb_2Se_3/CdSe/Pt photoelectrode shows an approximate semicircle and a straight line. Considering the additional interface of CdSe, R(CR)(CR)W circuit are used to simulate the Nyquist plot of Sb_2Se_3/CdSe/Pt. The fitting values of all the electrochemical parameters are summarized in Table 2. A remarkably decreased R_{ct} value of 224.0 Ω is observed for Sb_2Se_3/CdSe/Pt electrode as against 1904 Ω for Sb_2Se_3/Pt. Thus, CdSe coating could facilitate the charge transfer of Sb_2Se_3 layer, thereby improving the photocurrent response. Generally, a lower characteristic peak frequency in Bode phase plots indicates a longer electron lifetime.[29,30] As shown in the Fig. 3e, Sb_2Se_3/CdSe/Pt photocathode exhibits a lower characteristic peak frequency (1.8 Hz) than the Sb_2Se_3/Pt photocathode (21.5 Hz), indicating the longer electron lifetime and, therefore, lower carrier recombination rate.

Moreover, Mott–Schottky analysis was conducted on Sb_2Se_3/Pt and Sb_2Se_3/CdSe/Pt electrodes to explore the interface energetics. The negative slope of the Mott–Schottky plots for both samples confirms the p-type semiconductor character of Sb_2Se_3 (Fig. 3f). Besides, carrier concentration increases significantly for Sb_2Se_3/CdSe/Pt electrode, compared to Sb_2Se_3/Pt (Table S2), implying the enhanced charge transport due to the formation of Sb_2Se_3/CdSe heterojunction.[31] The flat band potential (E_{fb}) can be determined by the *x*-intercept of the linear region of the Mott–Schottky plots. The Sb_2Se_3/CdSe/Pt photoelectrode exhibits an E_{fb} value of 0.75 V_{RHE}, which is positively shifted by 150 mV relative to that of the Sb_2Se_3/Pt photocathode (0.6 V_{RHE}). This positive shift in E_{fb} agrees with the anodic shift in onset potentials (Fig. 3a), demonstrating enhanced driving force for interfacial charge separation and transfer.[32]

The stability was evaluated by a long-time current–time test. The photocurrent of Sb_2Se_3/Pt and Sb_2Se_3/CdSe/Pt photocathodes decreased gradually from −0.11 to 0.06 mA cm^{-2} and −0.56 to −0.41 mA cm^{-2} respectively with a rapid decay in the first few minutes (Fig. S10). The photocurrent retained 73.2% of the initial value for Sb_2Se_3/CdSe/Pt photocathode after one hour of testing, showing a better photostability. XPS measurements were performed to probe the chemical species and chemical bonding state. By comparing the Sb 3d spectra (Fig. S11a) of the

Table 2 Electrochemical parameters of photoelectrodes obtained from EIS study

Samples/parameters	R_s/Ω	R_{ct}/Ω	CPE_1/μF cm^{-2}	R_1/Ω	CPE_2/μF cm^{-2}
Sb_2Se_3/Pt	70.24	1904	55.78	—	—
Sb_2Se_3/CdSe/Pt	59.26	224.0	20.61	10.84	11.83

electrodes before and after testing, it can be seen that the peak area corresponding to O 1s increases remarkably, which is likely related to the precipitation of Sb_2O_3 on the film.[33] The Se 3d signal of the sample (Fig. S11b) before stability test can be fitted into two pairs of typical peaks, indicating the presence of $Se^{2-}$and Se^0 species.[34] After testing, the Se^0 species disappeared and the peak area ratio of Se^{2-} reduced, showing that the loss of Se element occurs during testing. The peaks at 405.4 eV and 412.2 eV represent the Cd $3d_{5/2}$ and Cd $3d_{3/2}$ of Cd^{2+} (Fig. S11c), respectively, which are positively shifted after the stability test. These results indicate that the Se species is not stable, which results in the decay of photocurrent.

To investigate the effect of Sb_2Se_3/CdSe heterojunction on charge separation, the band structure of the Sb_2Se_3 and CdSe is carefully proposed. Before contact, the Fermi level of Sb_2Se_3 is near the valence band (VB) maximum. Based on the E_{fb} (Fig. 2d) and bandgap energy, the Fermi level, VB and conduction band (CB) are determined to be 5.08, 5.28 and 3.94 eV, respectively. According to the previous reports, CdSe behaves as a typical n-type semiconductor with the Fermi level, CB and VB positioned at 4.47, 4.35 and 6.07 eV,[35] respectively (Fig. 4a). After forming p–n heterojunction, the Fermi levels of Sb_2Se_3 and CdSe equilibrate (Fig. 4b). Under illumination, photoexcited electrons in Sb_2Se_3 migrate to the CB of CdSe, while holes from CdSe are promptly captured by the VB of Sb_2Se_3 (Fig. 4c). The accumulated electrons at CdSe are then channeled to Pt cocatalyst for H_2 production, simultaneously suppressing the recombination of carriers and enhancing interfacial charge transfer, ultimately boosting PEC activity.

3.4 Effect of electrodeposited charge densities on PEC properties of Sb_2Se_3-Based electrodes

To investigate the influence of the thickness of light absorption layer on the performance, we fabricated the Sb_2Se_3/CdSe photocathode started with the deposition of Sb_2Se_3 layers by changing electrodeposited charge densities (0.125–1.0C cm^{-2}). The cross-sectional microstructure of 0.125, 0.25, and 0.5C cm^{-2} Sb_2Se_3/CdSe samples were observed by SEM (Fig. S12). It can be seen that with larger electrodeposited charge density, the Sb_2Se_3 layer becomes thicker, varying from 102 nm to 140 nm. The influence of charge density during electrodeposition on the PEC performance is illustrated in Fig. 5a. The largest photocurrent density of −6.9 mA cm^{-2} at −0.2 V_{RHE} was achieved for the electrode that was electrodeposited for 0.25C cm^{-2}. The decreased photocurrent density was observed for the thicker light-absorption layer-based device, with a photocurrent density of −2.8 mA cm^{-2} at −0.2 V_{RHE}.

Fig. 5b shows the absorption spectra of samples with different thickness. According to the transmittance and reflectance spectra of Sb_2Se_3 layer with different thickness (Fig. S13), the thick Sb_2Se_3 layer can absorb more photons than the thin counterpart (Fig. 5a). Hence, the reduced photocurrent for thin Sb_2Se_3 layer is likely related to the reduced carrier production. Blue and green photons with a wavelength of 375–600 nm are mostly absorbed close to the Sb_2Se_3/CdSe interface.[12,21] Photoexcited holes in this region need to travel a long distance to reach the back contact. Given the inherently low mobility and diffusion length of hole relative to that of electron for Sb_2Se_3, the thick Sb_2Se_3 layer photoelectrode likely suffers from sluggish hole diffusion kinetics, thereby diminishing overall carrier collection efficiency.

Moreover, EIS was performed to clarify the origin of the decreased photocurrent density for the thick Sb_2Se_3 layer-based cell. As indicated by the Nyquist plot (Fig. 5c) and the fitting results (Table S3), the thinnest and worst-performing electrode (102 nm thick sample) shows the largest R_{ct} (6.6 k Ω), while the corresponding R_{ct} for the 126 nm thick (0.25C cm^{-2}) sample is

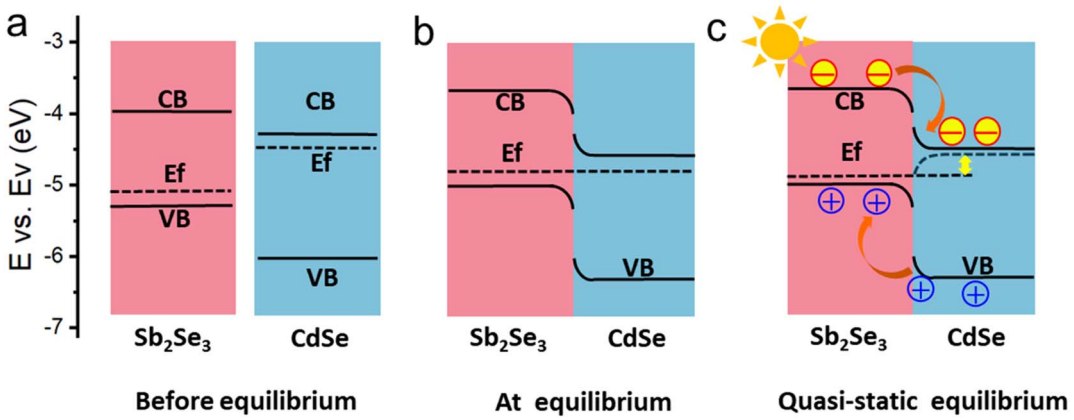

Fig. 4 Schematic energy level alignment (a) before equilibrium, (b) at equilibrium and (c) quasi–static equilibrium of Sb_2Se_3 and CdSe films.

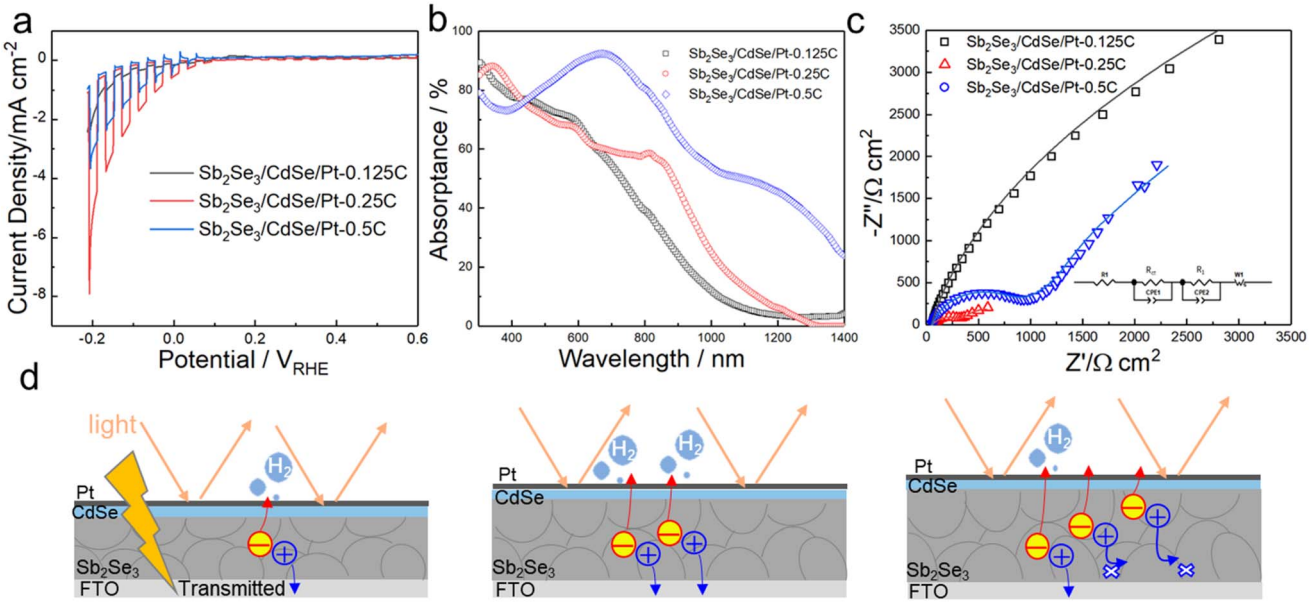

Fig. 5 (a) Current–potential curves of photocathodes deposited with different charge densities. (b) Absorption spectra and (c) Nyquist plots for the as-obtained samples. (d) Schematics of the photo absorption and carrier transport in the PEC devices based on Sb_2Se_3 films with different thicknesses.

the smallest (0.2 k Ω, respectively), which explains for the higher photocurrent density of the film prepared by passing 0.25C cm^{-2} charge density in comparison to the other electrode. As the thickness increases further, a larger resistance was observed (0.7 k Ω). Experimental results reveal that merely increasing the thickness of absorber layer for better light absorption was ineffective for enhancing the photocurrent of the PEC device. As illustrated in Fig. 5d, the charge-transport process and optical absorption in the PEC device strongly depends on the absorber thickness. Too thick absorber layer could lead to the poor charge transport and too thin absorber layer could results in insufficient light absorption. An appropriate thickness of the absorber layer allows sufficient absorption as well as efficient charge transport without recombination.

4. Conclusions

In summary, a novel Sb_2Se_3/CdSe p–n heterojunction was successfully fabricated by a facile electrodeposition followed by annealing and surface modification. Factors affecting the photoelectrochemical activity such as the annealing temperature and electrodeposited charge density have been investigated and optimized. The Sb_2Se_3/CdSe/Pt photocathode with Sb_2Se_3 electrodeposited for 0.25C cm^{-2} and annealed at 250 °C exhibits the optimal performance. The fabricated PEC device achieves a photocurrent density of *ca.* −6.9 mA cm^{-2} at −0.2 V_{RHE} in near-neutral solution, which is 2.3 times higher than the Sb_2Se_3/Pt. The enhanced photoelectrochemical performance is owing to the successful construction of Sb_2Se_3/CdSe p–n heterojunction, which contributes to effective charge separation and transfer. This study demonstrates the potential of Sb_2Se_3-based low-band-gap photocathode for scalable solar hydrogen production, although a further improvement in the photocurrent density and stability through additional interface engineering is required.

Author contributions

Liting Wei: funding acquisition, data curation, formal analysis, investigation, writing – original draft, writing – review & editing. Yinhu Yu: formal analysis, investigation, writing – review & editing. Tong Chang: writing – review & editing Jiao Jiao: writing – review & editing. Yangfang Wu: writing – review & editing.

Conflicts of interest

The authors declare that they have no known competing financial interests or personal relationships that could have appeared to influence the work reported in this paper.

Data availability

The data that support the findings of this study are available from the corresponding author upon reasonable request.

Supplementary information (SI): XRD patterns, SEM images of photoelectrodes, Tauc plots, light-harvesting efficiency curves, integrated photocurrent density, stability tests, and fitting results of Nyquist plots. See DOI: https://doi.org/10.1039/d6ra00129g.

Acknowledgements

This work is supported by the Doctoral Research Initiation Project of Yuncheng University, China (No. YXBQ-202516) and

Basic Research Program of Yuncheng City, China (No. YCKJYD-202538).

References

1 S. A. Lee, S. Choi, C. Kim, J. W. Yang, S. Y. Kim and H. W. Jang, *ACS Mater. Lett.*, 2019, **2**, 107–126.
2 J. Ke, F. He, H. Wu, S. Lyu, J. Liu, B. Yang, Z. Li, Q. Zhang, J. Chen, L. Lei, Y. Hou and K. Ostrikov, *Nano-Micro Lett.*, 2020, **13**, 24.
3 Y. Zhou, L. Wang, S. Chen, S. Qin, X. Liu, J. Chen, D.-J. Xue, M. Luo, Y. Cao, Y. Cheng, E. H. Sargent and J. Tang, *Nat. Photonics*, 2015, **9**, 409–415.
4 Z. Li, X. Liang, G. Li, H. Liu, H. Zhang, J. Guo, J. Chen, K. Shen, X. San, W. Yu, R. E. I. Schropp and Y. Mai, *Nat. Commun.*, 2019, **10**, 125.
5 K. Zeng, D.-J. Xue and J. Tang, *Semicond. Sci. Technol.*, 2016, **31**, 063001.
6 G. Ghosh, *J. Phase Equilib.*, 1993, **14**, 753–763.
7 S. Siebentritt, M. Igalson, C. Persson and S. Lany, *Prog. Photovoltaics*, 2010, **18**, 390–410.
8 S. Chen, A. Walsh, X.-G. Gong and S.-H. Wei, *Adv. Mater.*, 2013, **25**, 1522–1539.
9 W. Yang and J. Moon, *J. Mater. Chem. A*, 2019, **7**, 20467–20477.
10 J. Park, W. Yang, Y. Oh, J. Tan, H. Lee, R. Boppella and J. Moon, *ACS Energy Lett.*, 2019, **4**, 517–526.
11 H. Lee, W. Yang, J. Tan, Y. Oh, J. Park and J. Moon, *ACS Energy Lett.*, 2019, **4**, 995–1003.
12 J. Park, W. Yang, J. Tan, H. Lee, J. W. Yun, S. G. Shim, Y. S. Park and J. Moon, *ACS Energy Lett.*, 2019, **5**, 136–145.
13 L. Zhang, Y. Li, C. Li, Q. Chen, Z. Zhen, X. Jiang, M. Zhong, F. Zhang and H. Zhu, *ACS Nano*, 2017, **11**, 12753–12763.
14 Y. Li, K. Wang, D. Huang, L. Li, J. Tao, N. A. A. Ghany and F. Jiang, *Appl. Catal. B Environ. Energy*, 2021, **286**, 119872.
15 X. Wen, C. Chen, S. Lu, K. Li, R. Kondrotas, Y. Zhao, W. Chen, L. Gao, C. Wang, J. Zhang, G. Niu and J. Tang, *Nat. Commun.*, 2018, **9**, 2179.
16 D. B. Li, X. X. Yin, C. R. Grice, L. Guan, Z. N. Song, C. L. Wang, C. Chen, K. H. Li, A. J. Cimaroli, R. A. Awni, D. W. Zhao, H. S. Song, W. H. Tang, Y. F. Yan and J. Tang, *Nano Energy*, 2018, **49**, 346–353.
17 K. R. Tolod, S. Hernández, M. Castellino, F. A. Deorsola, E. Davarpanah and N. Russo, *Int. J. Hydrogen Energy*, 2020, **45**, 605–618.
18 Y. Cheng, Q. Sun, Q. Li, W. Zhang, E. Liu, J. Fan, H. Xie, H. Miao and X. Hu, *Sci. China Mater.*, 2022, **66**, 1460–1470.
19 J. Tan, W. Yang, Y. Oh, H. Lee, J. Park, R. Boppella, J. Kim and J. Moon, *Adv. Energy Mater.*, 2019, **9**, 1900179.
20 Z. Wang, T. D. Nguyen, L. P. Yeo, C. K. Tan, L. Gan and A. I. Y. Tok, *Small*, 2020, **16**, e1905826.
21 T. T. Ngo, S. Chavhan, I. Kosta, O. Miguel, H.-J. Grande and R. Tena-Zaera, *ACS Appl. Mater. Interfaces*, 2014, **6**, 2836–2841.
22 L. Zhang, Y. Li, C. Li, Q. Chen, Z. Zhen, X. Jiang, M. Zhong, F. Zhang and H. Zhu, *ACS Nano*, 2017, **11**, 12753–12763.
23 T. S. Shyju, S. Anandhi, R. Indirajith and R. Gopalakrishnan, *J. Alloys Compd.*, 2010, **506**, 892–897.
24 K. Sun, C. Yan, F. Liu, J. Huang, F. Zhou, J. A. Stride, M. Green and X. Hao, *Adv. Energy Mater.*, 2016, **6**, 1600046.
25 L. He, W. Zhou, L. Hong, D. Wei, G. Wang, X. Shi and S. Shen, *J. Phys. Chem. Lett.*, 2019, **10**, 2278–2285.
26 J. Kim, W. Yang, Y. Oh, H. Lee, S. Lee, H. Shin, J. Kim and J. Moon, *J. Mater. Chem. A*, 2017, **5**, 2180–2187.
27 S. Chen, Y. Chen, H. S. Aziz, H. H. Zhang, Z. L. Li, Y. X. Chen, Y. J. Zeng, Z. H. Zheng, J. G. Hu, Z. H. Su and G. X. Liang, *Adv. Funct. Mater.*, 2024, **35**, 2420912.
28 S. Chen, Y. Chen, H. Zhang, M. Abbas, D. Ren, Y. Chen, J. Luo, Z. Zheng, Z. Su and G. Liang, *Adv. Mater.*, 2026, **38**, 202518202.
29 R. Fan, J. Zhou, W. Xun, S. Cheng, S. Vanka, T. Cai, S. Ju, Z. Mi and M. Shen, *Nano Energy*, 2020, **71**, 104631.
30 C. Chen, Y. Lu, R. Fan and M. Shen, *ChemSusChem*, 2020, **13**, 3893–3900.
31 P. Kuang, L. Zhang, B. Cheng and J. Yu, *Appl. Catal. B Environ. Energy*, 2017, **218**, 570–580.
32 X. Chen, Z. Yin, K. Cao and S. Shen, *ACS Mater. Lett.*, 2022, **4**, 1381–1388.
33 M. B. Costa, F. W. S. Lucas, M. Medina and L. H. Mascaro, *ACS Appl. Energy Mater.*, 2020, **3**, 9799–9808.
34 Y. Zhang, S. Li, L. Cheng, Y. Li, X. Ren, P. Zhang, L. Sun and H. Y. Yang, *J. Mater. Chem. A*, 2021, **9**, 3388–3397.
35 K. Li, X. Lin, B. Song, R. Kondrotas, C. Wang, Y. Lu, X. Yang, C. Chen and J. Tang, *Front. Optoelectron.*, 2021, **14**, 482–490.